Journal of
Materials Chemistry A

Accepted Manuscript

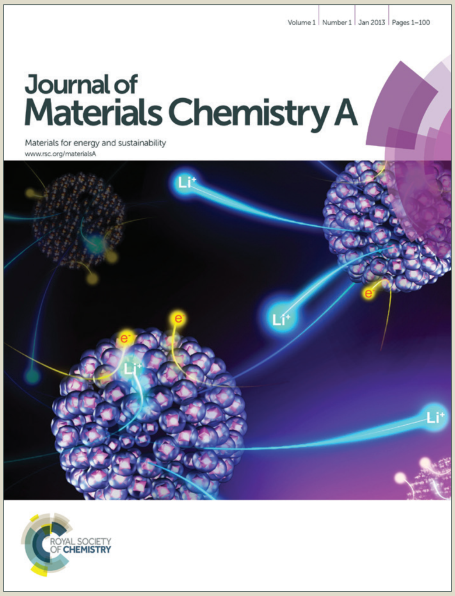

ROYAL SOCIETY
OF **CHEMISTRY**

www.rsc.org/materialsA

Journal of Materials Chemistry A RSCPublishing

ARTICLE

Cite this: DOI: 10.1039/x0xx00000x

Received 00th January 2014,
Accepted 00th January 2014

DOI: 10.1039/x0xx00000x

www.rsc.org/

Photoelectrochemical and electrocatalytic properties of thermally oxidized copper oxide for efficient solar fuel production

Angel T. Garcia-Esparza,[a]‡ Kevin Limkrailassiri,[b]‡ Frederic Leroy,[c] Shahid Rasul,[a] Weili Yu,[a] Liwei Lin[b] and Kazuhiro Takanabe[a]*

We report the use of a facile and highly scalable synthesis process to control growth products of earth-abundant Cu-based oxides and their application in relevant photoelectrochemical and electrochemical solar fuel generation systems. Characterizations of the synthesized Cu(I)/Cu(II) oxides indicate that their surface morphology and chemical composition can be simply tuned by varying two synthesis parameters (time and temperature). UV-Vis spectroscopy and impedance spectroscopy studies are performed to estimate the band structures and electronic properties of these *p*-type semiconductor materials. Photoelectrodes made of Cu oxides possess favorable energetic band structures for hydrogen production from water; the position of their conduction band is ≈ 1 V more negative than the water-reduction potential. High acceptor concentrations on the order of 10^{18}-10^{19} cm^{-3} are obtained, producing large electric fields at the semiconductor-electrolyte interface and thereby enhancing charge separation. The highly crystalline pristine samples used as photocathodes in photoelectrochemical cells exhibit high photocurrents under AM 1.5G simulated illumination. When the samples are electrochemically reduced under galvanostatic conditions, the co-existence of the oxide with metallic Cu on the surface seems to function as an effective catalyst for the selective electrochemical reduction of CO_2.

Introduction

The sustainable creation of fuels from solar power is a promising renewable-energy technology that harnesses sunlight for the production of hydrogen/hydrocarbon from water/CO_2 feedstock *via* the photocatalytic dissociation of water and the (photo)-electrocatalytic reduction of CO_2, respectively.[1] Growing interest in solar energy has arisen from global concern over depleting fossil-fuel reserves and irreparable damage to the environment caused by greenhouse-gas emissions. Among all forms of solar energy, water splitting has the advantage of capturing sunlight, an intermittent energy resource, and storing it in the form of a chemical bond, H_2, which can be burned and utilized as electricity on demand.[2,3] Moreover, the wide-scale implementation of solar and other renewable sources of energy requires an improved means of energy storage, such as the reduction of CO_2 to CO or energy-rich hydrocarbons.[4] CO_2 must be introduced as a key component in the value chain of chemical industries.[5,6] For solar fuel production to provide a clean, abundant source of renewable energy that is also competitively priced compared to current energy resources, scalable processing methods and earth-abundant starting materials will be required.[2]

To this end, metal-oxide semiconductors have emerged as desirable materials for the working electrodes in photoelectrochemical (PEC) cells and as catalysts for (photo)-electrochemical CO_2 reduction.[4,7] Of the metal oxides, cuprous oxide (Cu_2O) has gained particular attention for PEC water splitting because of the earth abundance of the metal.[8] Generally, Cu_2O exhibits *p*-type semiconductivity with a reported 2.0 eV direct band gap, making this material highly attractive as a photocathode for the direct generation of hydrogen from water.[9] On the basis of its band-gap energy, Cu_2O has a maximum conversion efficiency of 18% and a maximum theoretical photocurrent of 14.7 mA cm^{-2}.[10] Paracchino *et al.* have reported a photocurrent for Cu-oxide-based photoelectrodes of −7.6 mA cm^{-2} at 0 V *vs.* a reversible hydrogen electrode (RHE) using electrodeposited Cu_2O and protected the photocathode with carefully tuned oxide multi-layers of ZnO (4 nm) and Al_2O_3 (0.17 nm) followed by an 11 nm TiO_2 film decorated with a Pt cocatalyst. Although a significant contribution to the reported photocurrents in the literature originates from the reduction of Cu_2O, they and others have proved that when a protection strategy was applied, significant amounts of hydrogen were generated by the oxide photocathode.[8,11] The synthesis of Cu_2O photocathodes is generally achieved through electrochemical deposition

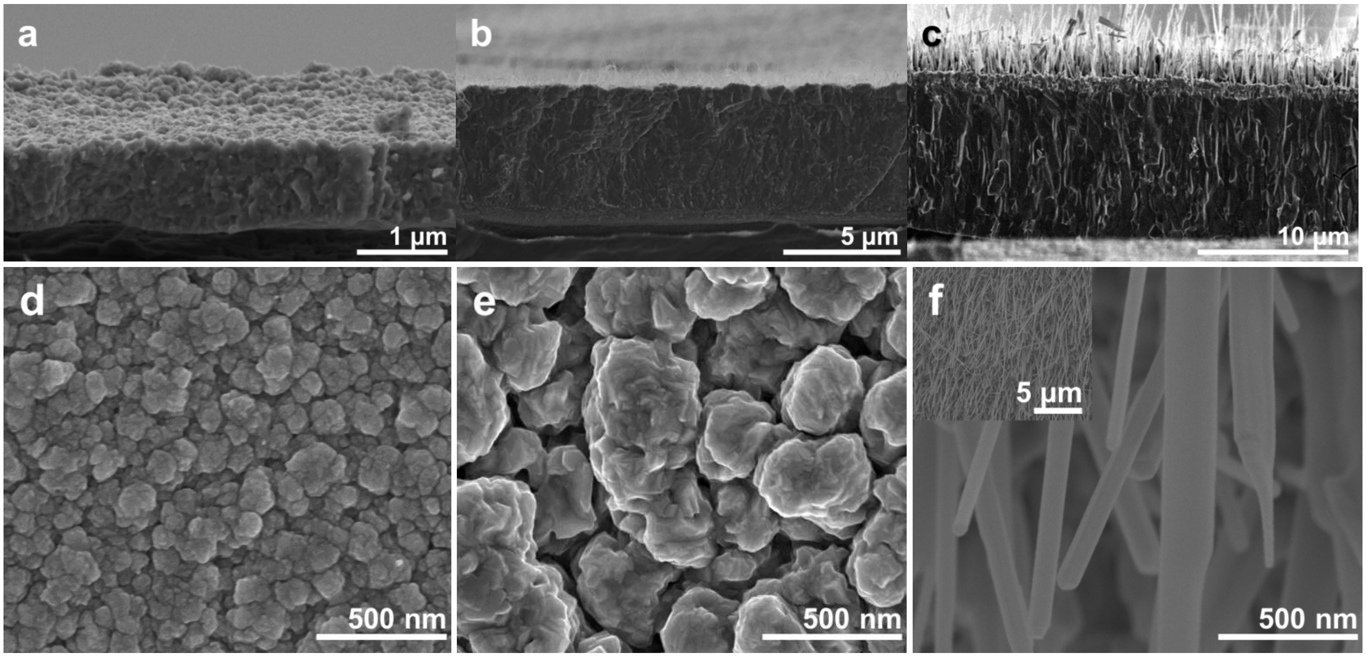

Fig. 1 The top and cross-sectional SEM views of (a, d) the red sample treated at 573 K for 0.5 h, (b, e) the deep red sample treated at 573 K for 10 h and (c, f) the black sample treated at 773 K for 2 h.

methods,[10,12,13] physical deposition techniques,[14,15,16] the electrochemical anodization of Cu[17,18], and solution-phase methods.[19,20] However, the reliable, scalable and mass-producible synthesis of high-quality *p*-type semiconductors that can efficiently drive the half-reaction of hydrogen production remains an important challenge.[21]

In contrast, the development of efficient CO_2 conversion is desired because of the growing environmental concerns regarding greenhouse gas emissions.[22] It is well known that polycrystalline Cu metal catalyzes the electrochemical reduction of CO_2 to higher hydrocarbons more actively than other metals. However, this activity comes at the expense of the large overpotential that is required to favor CO_2 reduction over hydrogen evolution. Recently, it has been reported that copper oxides and other metal oxides exhibit higher selectivities than metal electrodes for electrochemical CO_2 reduction.[23,24] The selective design of the metal-oxide surface composition remains an important scientific challenge for the practical large-scale application of the electrocatalysis of CO_2 reduction.

In this work, we report on the use of a facile synthesis procedure to make highly crystalline *p*-type Cu_2O semiconductors by thermal oxidation of copper foils with and without CuO nanowires on their surfaces. In these composite materials, the semiconductor is in intimate ohmic contact with the Cu substrate. Here, we focus on understanding the intrinsic nature of the copper-based composites synthesized in this manner, which have attracted tremendous interest for potential scalable applications. For PEC and electrocatalytic applications, it is essential to understand the redox properties and the semiconductive nature of these Cu-oxide-based composites. Systematic studies were conducted using electrochemical characterizations, PEC measurements, impedance spectroscopy and the electrocatalytic reduction of CO_2. In the PEC measurements, the pristine, as-processed planar Cu-oxide-based semiconductor photocathodes achieved high photocurrents under simulated air-mass 1.5 global irradiation (AM 1.5G). Remarkably, the sample produced at higher temperature (773 K, 2 h) exhibited onset potentials of approximately 0.8 V *vs*. RHE generating ≈ 1 mA cm^{-2} photocurrents at a positive potential of 0.5 V *vs*. RHE. Furthermore, the synthesis of the photocathodes was highly reproducible because of the simplicity of the synthesis procedure, fulfilling a prerequisite for the possibility of high-yield mass production in the future. In the electrochemical CO_2 reduction reaction, CuO_x reduction was found to be essential before CO_2 conversion. Given that pure metallic copper does not facilitate CO_2 reduction under the same conditions (i.e., H_2 evolution is favored), thorough characterization revealed that the coexistence of metal and oxidized copper appears to be beneficial for CO_2 reduction.

Results and discussion

Cu-based electrodes were prepared from high-purity Cu foil with a 25 μm thickness, which was cut into samples of 1.0 cm by 3.0 cm, cleaned and subjected to different thermal-oxidation treatments. The representative electrodes are further discussed below, and they were prepared using three different time and temperature combinations during oxidation: 573 K for 0.5 h (henceforth referred to as the "red" samples for convenience), 573 K for 10 h ("deep red") and 773 K for 2 h ("black"). The cross-sectional and top-view SEM micrographs of the red sample are shown in Figures 1a and 1d (also see Figures S1a and S1b). The granular surface contains particles ranging from 100 to 300 nm in diameter. Grains with a similar diameter can be observed in the cross section along with voids interspersed between the grains. This layer was confirmed to be Cu_2O on the basis of the X-ray diffraction (XRD) pattern shown in Figure 2. The thickness of the Cu_2O layer in the red sample was estimated to be 1 μm. Increasing the oxidation time from 0.5 to 10 h expanded the diameters of the surface particles to 400 to 1000 nm and led to the formation of more crystalline and void-free Cu_2O (Figures 1b and 1e and supplementary Figures S1c

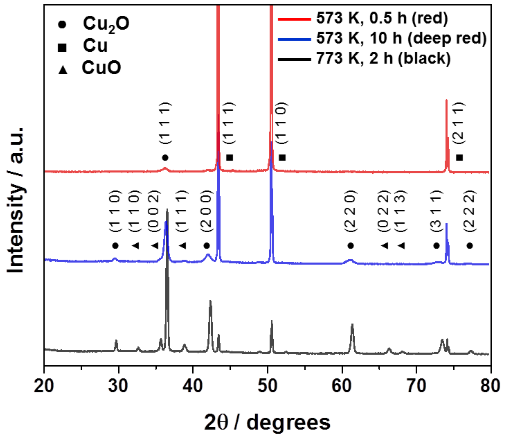

Fig. 2 XRD diffractograms of samples treated under different thermal-oxidation conditions, coded as the red, deep red and black samples.

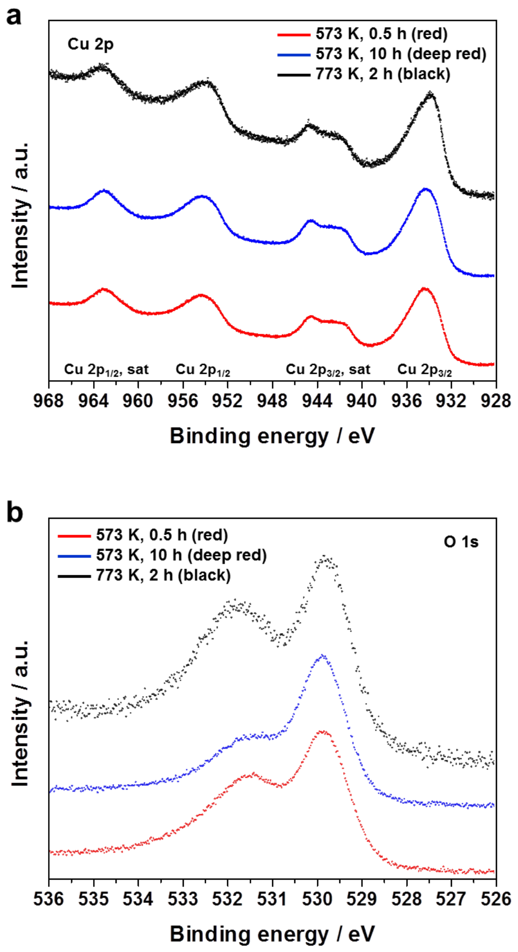

Fig. 3 Core-level (a) Cu 2p and (b) O 1s XPS spectra for the pristine Cu-based samples.

and S1d). This treatment also led to the onset of CuO growth, as indicated by the nanowire structures on the Cu_2O surface in Figure 1b. The cupric oxide phase was also confirmed *via* XRD and X-ray photoelectron spectroscopy (XPS, *vide infra*). The CuO nanowire growth on the deep red sample is sparse compared to the black samples, whose top views are shown in Figure 1f and Figures S1e and S1f. The significant increase in CuO-nanowire growth at 773 K is consistent with other reports that such growth has been observed throughout the oxidation-temperature range of 773 to 973 K.[25] In the black sample, the nanowires average 8 µm in length and 50 to 150 nm in diameter. A ~400 nm layer of CuO at the base of the nanowires can be distinguished from the darker underlying Cu_2O in the cross section of the black sample shown in Figure 1c. The thickness of the Cu_2O layer increases from 1 µm (red) to ≈ 5 µm (deep red) to ≈ 10 µm (black). The weak CuO signals in the XRD pattern of the deep red and black samples, despite the highly dense growth of CuO nanowires on the latter, are attributed to the presence of a much thicker and more space-efficient Cu_2O layer. As expected, the XRD peaks display a decrease in the Cu signals and an increase in the Cu_2O signals while transitioning from the red sample to the deep red to the black (Figure 2). This observation is in agreement with the increased Cu consumption and conversion to Cu_2O observed with increasing oxidation time and temperature. The sharp Cu_2O (111) peak, the tallest of all the Cu_2O signals, suggests that the Cu_2O layer is highly crystalline and that this orientation was maximized. The (111) orientation has been reported to offer better hole collection efficiency, lower resistivity and higher carrier concentrations than (100)-oriented films.[26]

XPS was used to study the surface state of the pristine samples. Figure 3 presents the XPS spectra recorded for the oxidized Cu electrodes. The signals were corrected using the adventitious carbon peak C 1s at 284.8 eV as the reference. There were clear similarities in the analysis of the Cu 2p region for all samples, even though the thermal-oxidation treatment clearly affected the surface morphology and the oxide phase of the Cu-based materials, as first observed *via* SEM and indicated by the XRD results. In Figure 3a, the Cu 2p peaks are broad, thus making the unambiguous assignment of the oxidation states of Cu challenging. However, it is apparent that the surface contains mixed-valence higher oxidation states. The XPS signal of the red sample, in which the bulk XRD result shows no signs of CuO, exhibits broad Cu $2p_{3/2}$ and Cu $2p_{1/2}$ peaks with maxima at 933.9 and 953.8 eV, respectively, along with satellite peaks at 941.7, 944.4 and 963.0 eV. In fact, all of the samples reveal similar peak-maximum positions with an uncertainty of ±0.1 eV. The peaks located at 933.9 and 953.8 eV are assigned to the binding energies of Cu $2p_{2/3}$ and Cu $2p_{1/2}$, respectively, from Cu^{2+} on the surface.[27] Nevertheless, Cu^{+} with a reported doublet for Cu_2O located at 932.7 and 952.5 eV from Cu $2p_{2/3}$ and Cu $2p_{1/2}$, respectively, could explain the broadness of the observed peaks in these energy regions.[28,29] The detected satellite peaks at 941.7, 944.4 and 963.0 eV are in good agreement with the values reported in the literature, suggesting a partially filled Cu $3d^9$ shell, which confirms the presence of CuO on the surfaces of all electrodes.[29,30] In the red sample, Cu^{2+} may be present as a native cupric oxide layer that forms under the atmospheric conditions in which the sample was treated and subsequently exposed to air prior to the XPS measurement. This native oxide has been commonly reported to be 2 nm in thickness.[8] The subtle shoulder and the observed broadness toward higher binding energies for the Cu $2p_{3/2}$ signal of the black sample may be assigned to $Cu(OH)_2$ on the surface, which has a reported maximum of 934.7 eV. The formation of CuO nanowires was observed *via* SEM and confirmed *via* XRD for the deep red and black samples, and this finding is in agreement with the signals obtained from the Cu 2p XPS spectrum. The O 1s core-level XPS signal is presented in Figure 3b. Two broad peaks can be clearly identified for the samples, with apparent maxima at 529.9 and 531.5 eV. The former is assigned to CuO, and the latter, which has an extended broadness to 531.8 eV, can be attributed to ionically bonded hydroxide oxygen.[29] The O 1s signal for Cu_2O is generally found at 530.5±0.2 eV in the literature and may explain the broadness of the peak observed for all samples in Figure 3b.[29] The black sample exhibited a relatively broader O 1s peak at higher binding energies (≈ 531.5 eV), most likely caused by the overlapping signals attributed to chemisorbed water, chemisorbed hydroxyl oxygen and hydroxide oxygen.[27,29] Based on the bulk and surface characterizations, the Cu substrates are oxidized primarily to Cu_2O at temperatures below 673 K. Although a very thin native CuO layer forms at low temperatures in air, as revealed *via* XPS, a longer and more severe thermal-oxidation treatment (> 773 K) promotes the growth of a CuO layer on the surface of the Cu_2O, as indicated by the XRD, XPS and SEM observations. The growth of this layer may be kinetically limited, and the slow rate of formation of CuO ensures a low vapor pressure of this Cu(II) phase, thus creating nanowires with uniform diameters (Figure 1f and Figure S1f).[25] Based on the XPS and XRD results, the nanowires were confirmed to be CuO with a plausible $Cu(OH)_2$ layer on their surfaces.

To the naked eye, the surfaces of the black samples are far less reflective than those of the red and deep red samples; the black samples exhibit a dark, velvet-like appearance. UV-Vis diffuse reflectance spectra were transformed into the Kubelka-Munk function, as shown in Figure 4, revealing estimated band-gap energies of 2.07, 1.45 and 1.42 eV for the red, deep red and black samples, respectively (see the Tauc plots in Figure S2). The estimated band gaps are in agreement with the reported values for Cu_2O (2.0 eV) and CuO (1.4 eV).[8,10,12,31] The Tauc plots suggest the existence of an allowed direct transition near 2.08 eV for the red sample, which is assigned to Cu_2O and is in good agreement with the literature (Figure S2a).[10] The black sample exhibited a downward slope that is steeper than the slope of the deep red sample when the Tauc plot was analyzed in allowed-indirect-transitions mode (Figure S2b), which could possibly be attributed to the dense CuO on the surface of the black sample and is consistent with reports of CuO characterized as an indirect-band-gap *p*-type semiconductor.[14,32,33] The literature contains both allowed and forbidden direct transitions along with allowed indirect transitions near 2.0 eV for Cu_2O, in reasonable agreement with our results (Figure S2b).[3] Compared to the deep red and black samples, the red sample has a large background irrespective of the wavelength, most likely originating from a thicker underlying Cu layer as a result of the shorter oxidation time. Cu is reflective at long wavelengths, and therefore, photons are given additional opportunities to be absorbed by Cu_2O upon reflection from the Cu layer. At short wavelengths, Cu is absorptive, so the large Kubelka-Munk function can be attributed to absorption by both Cu_2O and Cu.

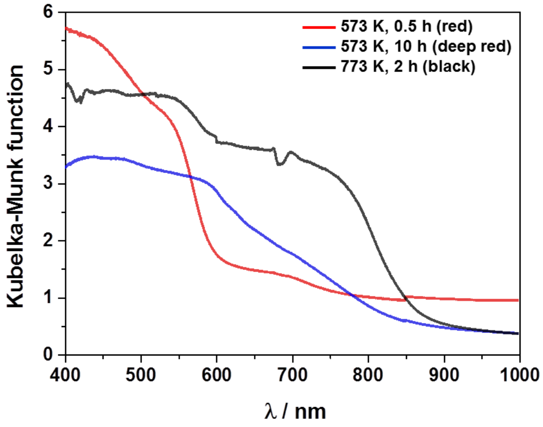

Fig. 4 Diffuse reflectance UV-Vis spectroscopy results transformed into the Kubelka-Munk function for the Cu-based red, deep red and black samples.

The electrochemical behavior of the Cu-based electrodes treated at different conditions was evaluated in 0.1 M sodium acetate electrolyte (pH 7.9) at 5 mV s^{-1}, and the results of two consecutive cycles are presented in Figures 5a, 5b and 5c for the red, deep red and black samples, respectively. Cyclic voltammetry (CV) experiments were used to evaluate the stability of the oxides under various applied potentials. When the potential range of the CV was limited from 0.5 to 0.8 V *vs.* RHE, no significant faradic currents were detected, and only double-layer capacitance was observed for all samples (black lines in Figures 5a to 5c). The CV results for the red sample are shown in Figure 5a; when the studied potential window was sufficiently large, three faradic processes were observed (AI, RI and RIII in Figure 5a). The CV was performed beginning from the open-circuit potential of the electrode and progressing toward more reducing conditions, and a cathodic signal appeared at potentials just above 0 V *vs.* RHE (RIII). Based on the SEM, XPS and XRD results, we assigned this cathodic current to the reduction of the relatively thin Cu_2O layer on the surface of the Cu electrode. This reduction wave is consistent with the literature.[8,34]

$$Cu_2O + H_2O + 2e^- \leftrightarrow 2Cu + 2OH^-$$

$$E° = 0.46\ \text{V}\ vs.\ \text{SHE} \qquad (1)$$

When the scanning direction was shifted toward more positive potentials, anodic processes were observed starting at 0.8 V *vs.* RHE. The polarization curve exhibited a broad anodic wave; this anodic current was attributed to the oxidation of metallic copper. Moreover, the broad anodic redox peak was not unambiguously resolved; thus, the simultaneous formation of cuprous oxide and cupric oxide and the possible dissolution of Cu^{2+} into solution were also considered.[35,36]

$$Cu_2O + H_2O \leftrightarrow 2CuO + 2H^+ + 2e^-$$

$$E° = 0.67\ \text{V}\ vs.\ \text{SHE} \qquad (2)$$

$$Cu_2O + 3H_2O \leftrightarrow 2Cu(OH)_2 + 2H^+ + 2e^-$$

$$E° = 0.73\ \text{V}\ vs.\ \text{SHE} \qquad (3)$$

On the next cycle, a new cathodic peak appeared centered at ≈ 0.7 V *vs.* RHE. The broad peak in Figure 5a (RI) may be assigned to the simultaneous reduction of both cuprous oxide and copper hydroxide to Cu_2O.[13,34] When the anodic scan was limited to 0.8 V *vs.* RHE (blue line in Figure 5a), the broad cathodic redox peak RI observed at ≈ 0.7 V *vs.* RHE disappeared. Only the reduction process at ≈ 0.1 V *vs.* RHE was detected (RIII), indicating that neither the formation of CuO nor the dissolution of copper occurred, and only the reduction of the Cu_2O layer was observed.[8] Figures 5b and 5c represent the

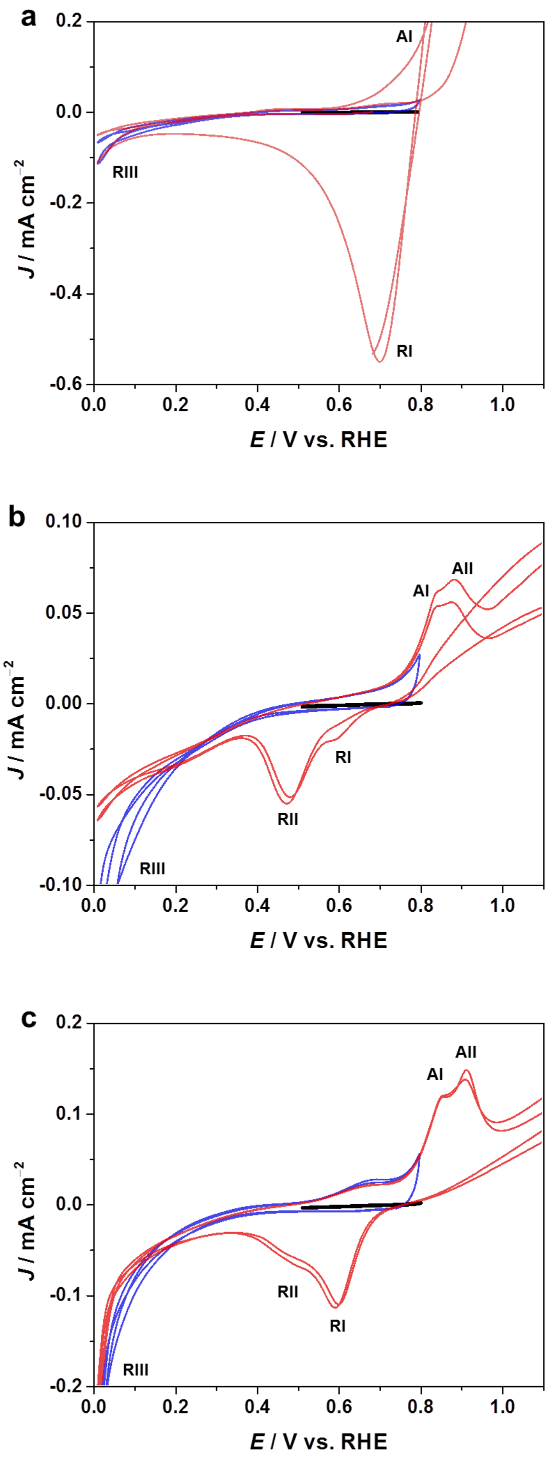

Fig. 5 Current-potential characteristics of the (a) red, (b) deep red and (c) black samples in the dark from the second and third cycles of the cyclic voltammetry experiments. A potential range limited to 0.5-0.8 V (black lines), 0.0-0.8 V (blue lines) or 0.0-1.2 V *vs*. RHE (red lines) was applied to study the redox reactions in the samples. (0.1 M sodium acetate, pH 7.9, 5 mV s^{-1}, Ar saturated)

CV experiments performed on the deep red and black samples, respectively. Note that the surfaces of the deep red and black samples are composed of two or three phases: Cu_2O and $CuO/Cu(OH)_2$, as previously discussed and confirmed *via* SEM, XRD, XPS and UV-Vis. The voltammograms obtained for both samples exhibit similar features, with two main anodic and two main cathodic redox peaks (AI, AII, RI and RII). For the anodic scan, the peak positions for both samples are the same: 0.85 (AI) and 0.90 (AII) V *vs*. RHE. Similarly, the positions of the cathodic peaks are the same for both samples: 0.59 (RI) and 0.49 (RII) V *vs*. RHE. This result may be an indication that the same redox reactions are occurring in both samples. When the potential scan of the deep red and black samples was limited to between 0 and 0.8 V *vs*. RHE, only the reduction wave RIII was observed (blue lines in Figures 5b and 5c). Nakayama *et al*. recently developed an electroanalytical method of elucidating the reduction mechanism of copper oxides using a strongly alkaline electrolyte.[37,38] They proved that under strong and weak alkaline conditions, the reduction of both oxides followed the same trend, in which the reduction of CuO was followed by the reduction of Cu_2O in one step toward the metallic state. It is therefore important to note the possibility of a one-step reduction for both Cu_2O and CuO in RIII (Equation 1 and 4).

$$\mathrm{CuO + H_2O + 2e^- \leftrightarrow Cu + 2OH^-} \qquad (4)$$

Large cathodic and anodic waves were detected at potentials more negative than 0.2 V *vs*. RHE and more positive than 1.0 V *vs*. RHE. As previously discussed, the former is assigned to the reduction of the copper oxides and the latter to the oxidation of Cu_2O.[8] Under the studied pH conditions, the third large anodic wave at high positive potentials has been attributed in the literature to the dissolution of Cu_2O, the probable formation of a metastable Cu_2O_3 phase just before oxygen evolution, or the plausible formation of a hydrated-polymeric form of cupric oxide.[35,39–41] The AI peak is assigned to the electro-oxidation of Cu metal and the formation of hydrous Cu_2O (the reverse reaction of Equation 1).[40] The AII peak is associated with the formation of complex hydrous CuO, most likely resulting in a duplex structure and forming a passive layer of $Cu(OH)_2$ on the surface of the sample (Equations 2 and 3).[40,41] The RI and RII peaks are assigned to the reduction of CuO (the reverse reaction of Equation 2) and the electrodeposition of Cu_2O from dissolved Cu^{2+} ions, respectively. The RI peak is in good agreement with the previously reported electrochemical characterizations of Cu_2O thin films obtained through electrodeposition.[8,42] There is a difference in the RI and RII reduction peaks between the deep red and black samples. The RI peak from the deep red electrode is smaller than the one observed for the black electrode. The opposite is observed for the R2 peak, where the area of the peak in the deep red sample is larger than the one recorded for the black sample. This result most likely arises because the black sample contains a larger amount of CuO on the surface, whereas in the deep red sample, Cu_2O may be exposed to the electrolyte (as indicated by the SEM and XPS results). Therefore, in the deep red sample, the oxidation of Cu_2O generates a higher concentration of Cu(II) cations dissolved in the electrolyte, increasing the charge of RII. The $CuO/(CuOH)_2$ in the black sample may function as a passivation layer reducing the dissolution process, and because the amount of CuO is larger, the RI redox peak for the reversible Equations 3 and 4 is more prominent, forming more Cu_2O from CuO.

Electrochemical impedance spectroscopy (EIS) was used to characterize the flat-band potentials of the samples and to estimate their intrinsic acceptor densities. A frequency scan from 0.01 Hz to 100 kHz at a fixed potential of 0.55 V *vs*. RHE

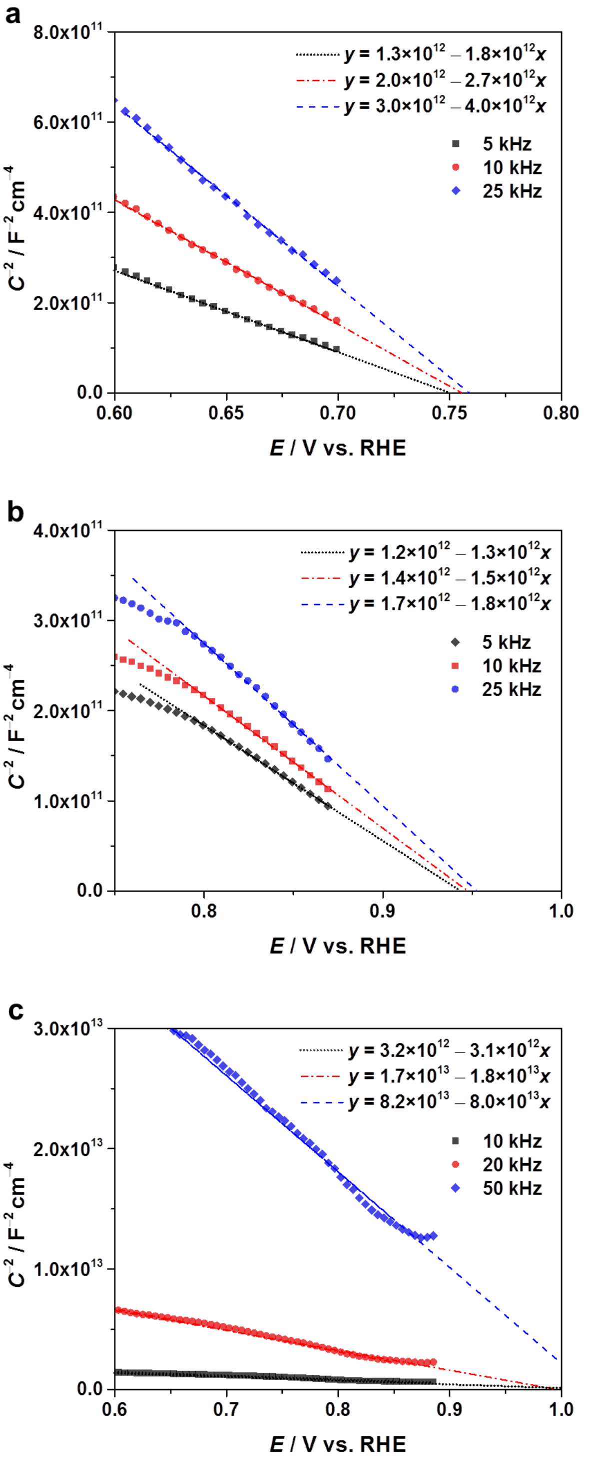

Fig. 6 Mott-Schottky plots in the dark of (a) red, (b) deep red and (c) black samples using a sinusoidal AC signal superimposed over the studied potential range with amplitude of 10 mV at high frequencies. (1-100 kHz, 0.1 M sodium acetate, pH 7.9, Ar saturated)

produced depressed semicircles in the Nyquist plot (Figure S3a). Thus, a modified Randles circuit using a constant-phase element was used to study the semiconductor-electrolyte interface.[43] The Mott-Schottky analysis was performed by sweeping the potential at fixed high frequencies with amplitude of 10 mV (1-100 kHz, Figure S4). The space-charge capacitance of the semiconductor was obtained from the imaginary part of the impedance, and the Mott-Schottky plots are presented in Figure 6. According to the Mott-Schottky equation, a linear fit produces a slope that can be used to approximate the majority-charge-carrier concentration, and by extrapolation, one can estimate the flat-band potential of the system.[10,43]

$$\frac{1}{C^2} = \frac{2}{A^2 e \varepsilon \varepsilon_0 N_A}\left(V - V_{fb} - \frac{k_B T}{e}\right) \qquad (6)$$

where C is the interfacial capacitance and V is the applied potential. Here, the constant A is the area, ε is the dielectric constant of the semiconductor, ε_0 is the permittivity of vacuum, T is the absolute temperature, e is the electronic charge, and k_B is the Boltzmann constant. As shown in Figure 6, a plot of C^{-2} versus potential may yield a straight line from which the flat-band potential (V_{fb}) and the carrier concentration (N_A) can be extracted. Based on the Mott-Schottky slopes, the samples demonstrated the characteristic *p*-type character of the oxide layers.[33,44] The extrapolated flat-band potentials are 0.75, 0.94 and 1.1 V *vs.* RHE for the red, deep red and black electrodes, respectively. For the red and deep red samples, minor frequency dependence can be observed from the slopes of the linear fits. This negligible effect most likely originates from contributions from the double-layer capacitance at the interface.[43] Nevertheless, for a dielectric constant of $\varepsilon_{r(\infty)} = 6.6$ for Cu_2O,[45] the carrier concentration can be reasonably estimated to be on the order of 10^{18} and 10^{19} cm^{-3} at high frequencies for the red and deep red samples, respectively. Based on the above estimations, we can further compute the maximum attainable electric field ($E_{\max}$) and the width of the space-charge region (W).[46]

$$E_{\max} = \frac{e N_A W}{\varepsilon \varepsilon_0} \qquad (7)$$

$$W = \sqrt{\frac{2\varepsilon\varepsilon_0 (V_{fb} - V)}{e N_A}} \qquad (8)$$

For the red sample, the calculations estimate a depletion width of 18 nm with an electric field of 8×10^5 V cm^{-1}. When the oxidation temperature increases (i.e., the deep red sample) the width of the space-charge layer is reduced to 7 nm, accompanied by an increase in the electric field to 3×10^6 V cm^{-1}. Assuming an effective hole mass of 0.58 m_0,[47] we can estimate the effective density of states for holes at the top of the valance band, N_V.[46] The computed acceptor concentration places the Fermi level at 61 and 2 meV above the valance band for the red and deep red samples, respectively. Based on the optical spectra, we can reasonably assume a 2.0 eV band gap for the Cu_2O layer and place the conduction band and valence band at −1.26 and 0.81 V *vs.* RHE, respectively, for the red sample. The relative band positions of the deep red sample are −1.13 and 0.94 V *vs.* RHE for its conduction and valence bands, respectively. These results demonstrate that the position of the conduction band of the composites is more negative (relative to the water-reduction potential) than is generally reported in the literature for electrochemically deposited copper oxides. In the specific case of the black sample (Figure 6c), there is a significant frequency dependence, which indicates that the rudimentary Randles circuit model may be insufficient

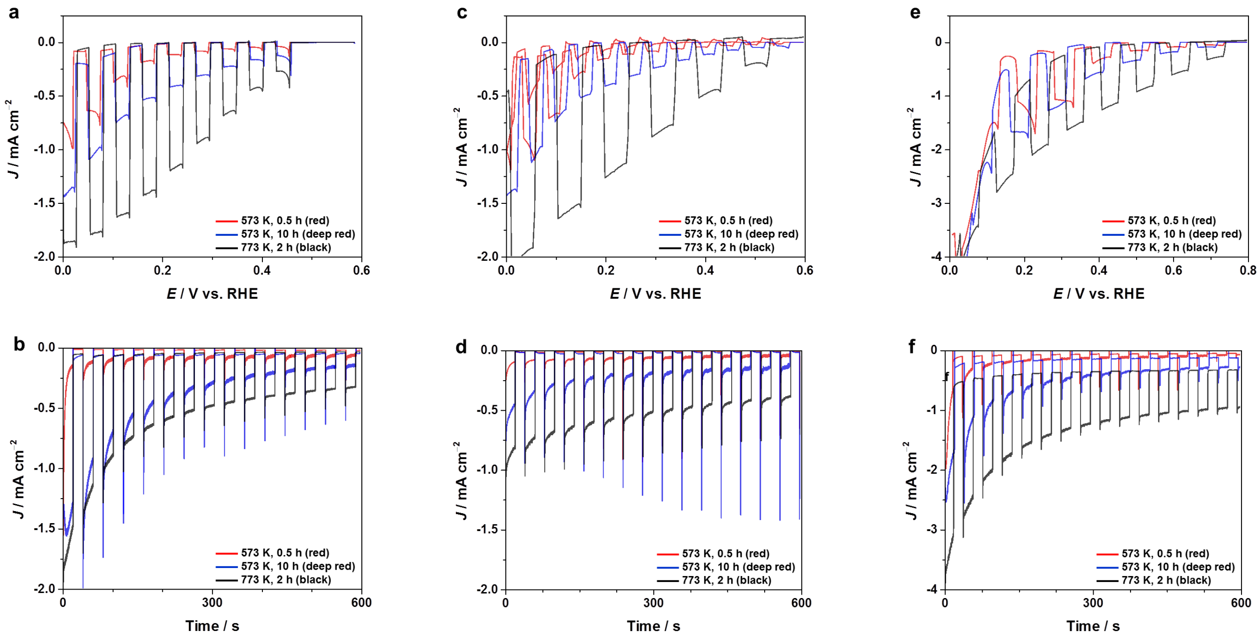

Fig. 7 Photoelectrochemical characterizations of red, deep red and black samples under simulated AM 1.5G solar irradiation at pH 4.9 (a and b), pH 6.1 (c and d) and pH 10.1 (e and f). The left-hand side shows the linear-sweep voltammetry under chopped illumination for the monitoring of the dark currents and photocurrents recorded for the Cu-based electrodes (a, c and e in 0.5 M Na_2SO_4, 10 mV s^{-1}, Ar saturated). The right-hand side represents the photoelectrochemical stability tests for the electrodes under 20 s illumination and dark periods at a constant potential of 0.25 V *vs*. RHE. (b, d and f in 0.5 M Na_2SO_4, Ar saturated)

to describe the complex interface found in this electrode.[3] We speculate that this sample may contain a larger density of low-energy surface/trap states, which generate localized levels in the forbidden region of the band gap.[48] Moreover, the high aspect ratio of the CuO nanowires on the black sample may introduce a significant double-layer capacitance component, making the calculation of the carrier density difficult. However, the Mott-Schottky results presented in Figure 6 display a similar trend: the fitted lines have different slopes at different frequencies, but all of the signals converge to the same flat-band potential intercept. Hence, these results yield accurate values for the extrapolation of flat-band conditions and reasonable carrier-concentration trends for the composite materials.[3] As mentioned before, the extrapolated flat-band potentials for the black samples are greater than 1 V *vs*. RHE (1.1±0.1 V *vs*. RHE), most likely as a result of the top ≈ 400 nm thick CuO layer at the interface. The obtained V_{fb} is in reasonable agreement with the values reported in the literature for CuO in contact with alkaline electrolytes.[44] Furthermore, this result implies the probable formation of a staggered *p-P* heterojunction in the black sample (see Figure S5 for an estimated energy-band diagram based on the above results).

The photoelectrochemical (PEC) characterization of the samples was evaluated in a three-electrode single-compartment cell with a Pt wire and an Ag/AgCl (saturated KCl) electrode as the counter and reference electrodes, respectively. Figure 7 presents the PEC current-potential characteristics of the samples under simulated AM 1.5G chopped illumination (Figure S6) in a 0.5 M Na_2SO_4 electrolyte under various pH conditions. The cathodic photocurrents were recorded for all samples and imply that the system exhibits band bending and a *p*-type nature, which is in agreement with the Mott-Schottky results and is attributed to the photo-assisted redox reactions at the semiconductor-electrolyte interface. The onset potentials of the photo-response of the samples at pH 4.9 (Figure 7a), pH 6.1 (Figure 7c) and pH 10.1 (Figure 7e) were estimated *via* extrapolation to be approximately 0.5, 0.6 and 0.8 V *vs*. RHE, respectively. Based on the impedance measurements, this trend is consistent with the observed increase in the flat-band potential position with increasing thermal-oxidation treatment. For a *p*-type photocathode, there is charge depletion at the interface that produces band bending and transports photoexcited electrons to the surface and holes into the bulk, toward the external circuit through the back contact and, finally, to the counter electrode, which drives the oxidation reaction.[10] Therefore, the extracted cathodic photocurrents originating from photoexcited electron-hole pairs are separated by the electric field at the semiconductor-electrolyte interface. At pH 10.1 and 6.1, the red and deep red samples exhibited similar responses at potentials close to 0 V *vs*. RHE (Figure 7c and 7e), whereas the black sample outperformed the other samples under all pH conditions. The largest photocurrents at pH 4.9 were recorded for the black and deep red samples, with average values of 1.8 and 1.4 mA cm^{-2}, respectively, under simulated solar illumination at 0 V *vs*. RHE. It is interesting to note that at pH 10.1, cathodic photocurrents of ≈ 1 mA cm^{-2} were observed from the black sample at positive potentials as high as 0.5 V *vs*. RHE. Based on our electrochemical characterization, negligible Cu redox reactions were detected at this potential (Figure 5). It is remarkable that in the absence of a cocatalyst (e.g., Pt), the reported photocurrents in the literature were generally found to be only several microamperes per square centimeter at 0.5 V *vs*. RHE.[11–13,41–45] The high crystallinity and intimate ohmic contact with the Cu substrate of Cu_2O may play a significant role in the reproducible large photocurrents observed for the deep red and black samples. Although the samples have different thicknesses which may produce higher resistance affecting charge transport, this effect was completely outweighed by other factors as measured photocurrents increase in the order of black > deep red > red sample. We can further attribute this high activity to a highly efficient charge separation induced by the large electric fields generated near the interface, which arise from the high carrier concentrations, as confirmed by the Mott-Schottky calculations.

The stability of the electrodes was studied in chronoamperometry experiments at a fixed potential of 0.25 V *vs*. RHE under chopped illumination periods of 20 s, and the results are presented in Figure 7 for various pH conditions. The initially high photocurrents were lost in less than 1 minute, as previously reported by other groups.[8,10,11,46] After 20 minutes of illumination, the samples exhibited stable photocurrents of 0.2, 0.08 and 0.05 mA cm^{-2} for the black, deep red and red samples, respectively, at both pH 4.9 and 6.1. Although increasing the pH appears to improve the stability of the materials, persistent dark currents were observed for the black electrode at 0.25 V *vs*. RHE under alkaline conditions (Figure 7e and 7f). Based on the photoelectrochemical characterization, it is probable that the photocathodes lost their activity because a significant percentage of the recorded photocurrents originate from the reduction of the Cu oxides on the surface, which are in contact with the electrolyte, as has been suggested in the literature (see Figure S7). Indeed, in our study we used an airtight single-compartment cell in a three-electrode configuration with online gas chromatography. We were unable to detect hydrogen although the corresponding photocurrents were within our detection limits of H_2 (0.1 mA cm^{-2}-equivalent), in agreement with other reports in the literature.[8,14,46] It was already demonstrated in the literature that once Cu_2O was protected from the electrolyte interface, the generated photoelectrons were efficiently collected in an energetically well aligned oxide-catalyst layer and hydrogen was produced inhibiting the reduction of the Cu_2O (i.e. Equation 1).[8,11] If a large number of the excited carriers generated under illumination are efficiently collected at the interface and selectively react with protons/water, the efficient production of hydrogen using our composite photocathode seems feasible. Surface protection becomes common strategy for Cu_2O and other semiconductor materials that are sensitive for photo-corrosion (i.e. multilayer oxide protection using SiO_2, Al_2O_3, ZnO, NiO, TiO_2, etc).[8,11,49,50,51,52,53] A stabilization strategy with a proper water-reduction catalyst similar to the multi-layer protection used recently by Paracchino *et al*. must be employed to obtain quantitative amounts of hydrogen from the system.[8,54]

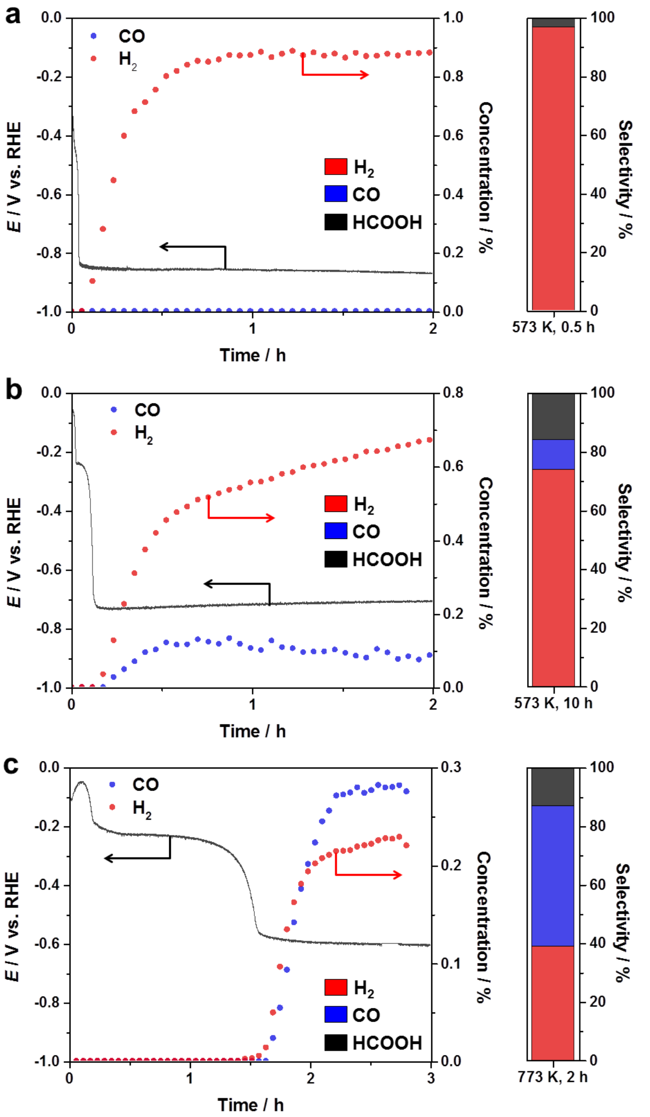

Fig. 8 Chronopotentiometric measurements at a constant current density of 1.67 mA cm^{-2} for the (a) red, (b) deep red and (c) black samples for the electrochemical reduction of CO_2. (0.1 M $KHCO_3$, CO_2 saturated, pH 6.8)

The Cu-based composite materials presented in this work could become versatile energy materials with a wide range of applications. Chronopotentiometry experiments with the samples at −1.67 mA cm^{-2} using online gas chromatography (μGC) measurements are presented in Figure 8. In the literature, when a Cu plate has been used as the catalyst for the electrochemical reduction of CO_2, a large overpotential (i.e., > 1 V *vs*. RHE) has been required for the production of hydrocarbons.[55] The red sample is a representative example that exhibits some similarities with the metallic case. When a constant current was applied to a red electrode in a two-compartment three-electrode electrolysis cell (0.1 M $KHCO_3$, CO_2 saturated, pH 6.8), a noticeable potential shift was observed during the first three minutes of the experiment (Figure 8a). During this transition time, the potential changed from 0.2 to −0.85 V *vs*. RHE. We attributed this change to the reduction of most of the oxide layer. Once the reduction was completed and the potential stabilized, we were able to detect steady rates of hydrogen gas evolution with selectivity greater than 90%. A similar trend was observed for all samples; the steady-state rates of gas generation were detected once the potential reached a stable value. Moreover, it was confirmed *via* high-pressure liquid chromatography (HPLC) that no liquid products were produced before the potential stabilized (Figure S8). The stabilization was achieved after 3, 9 and 120 minutes of galvanostatic experiments for the red, deep red and black samples, respectively, directly correlated with the different oxide thicknesses found in the samples (Figure 1). Interestingly, the potential reached a relatively stable value of −0.85 V *vs*. RHE for the red samples (Figure 8a), −0.7 V *vs*. RHE for the deep red (Figure 8b) and −0.6 V *vs*. RHE for the black (Figure 8c); the latter exhibited a considerable 250 mV shift in the overpotential required for the more selective reduction of CO_2 with respect to the red electrode (i.e., metallic-Cu behavior). A significant generation of CO was detected for the deep red and black samples. As the oxidizing thermal treatment increased, the selectivity for CO_2 reduction over H_2 production increased. The deep red sample exhibited 75% selectivity for generating H_2 while forming CO with 10% selectivity. The black sample exhibited 60% selectivity for CO_2 reduction under constant-current conditions (−1.67 mA cm^{-2}) with a recorded potential of −0.6 V *vs*. RHE. We further confirmed that when the temperature of the thermal treatment was held constant at 773 K and the treatment time was varied, no impact on the selectivity for carbon monoxide or formic acid was observed at a constant potential of −0.6 V *vs*. RHE (Table S1). Based on the above observations, when the thermally oxidized samples are further treated under galvanostatic conditions for different periods of time, the oxide layers are largely reduced, creating new and selective active sites for the electrochemical reduction of CO_2 that are stable.

The reduced Cu-based electrodes were characterized after the electrocatalytic reduction of CO_2. The surfaces of the electrodes were studied *via* XPS, and the results are presented in Figures 9a and 9b. The Cu 2p region clearly indicates a significant difference in comparison with the pristine samples (Figure 3a *vs*. Figure 9a). In all samples, the peaks in the XPS Cu 2p spectrum are shifted toward lower binding-energy values, indicating a more reduced state of the Cu species on the surface. The peak maxima are located at 933.0 and 952.9 eV for Cu $2p_{3/2}$ and Cu $2p_{1/2,}$ respectively. These results indicate the presence of Cu^+ and Cu^0 on the surfaces of the electrodes. An unambiguous assignment is not possible, therefore, there is the possibility of the existence of Cu_2O or some metastable oxide surface species.[23] No Cu $2p_{3/2}$ signals attributed to CuO were detected; nevertheless, there is a small broad signal in the black sample that appears in the characteristic satellite position assigned to Cu^{2+} in CuO (i.e., Cu $2p_{3/2}$, sat. at 944.6 eV). The O 1s spectrum is presented in Figure 9b. The peaks are significantly broader than those of the pristine samples because of the clear shift of the peak maxima toward 530.5 eV for the lower-binding-energy O 1s peak. As previously discussed, the second peak located at higher binding energies can be attributed to chemisorbed water or hydroxyl oxygen. Most importantly, it has been reported that the differentiation of copper species may involve the use of the O 1s line position.[27] In this case, the shift from 529.9 eV (Figure 3b) to 530.7 eV (Figure 9b) can be attributed to the presence of Cu^+ in the form of Cu_2O and the absence of CuO on the surface.[27,29] This result is most likely an indication of the existence of cuprous oxide in the vicinity of metallic copper on the surface after the electrocatalytic reaction under highly reducing conditions.

To clarify the extent of the reduction, bulk XRD diffractograms were obtained from the reduced samples, and the results are presented in Figure 9c. In contrast to the pristine samples, only Cu-metal diffractions were detected for the red and deep red samples, which is a possible indication of the consumption of the Cu_2O layer to produce Cu^0. Interestingly, the (111) and (220) Cu_2O diffractions remained in the black sample after the galvanostatic experiment. The Cu_2O diffractions in the black sample became smaller and broader after the electrochemical-reduction step, but the signals were not completely lost as in the case of the red and deep red samples, most likely because of the thicker and passivated $Cu_2O/CuO/Cu(OH)_2$ structure.

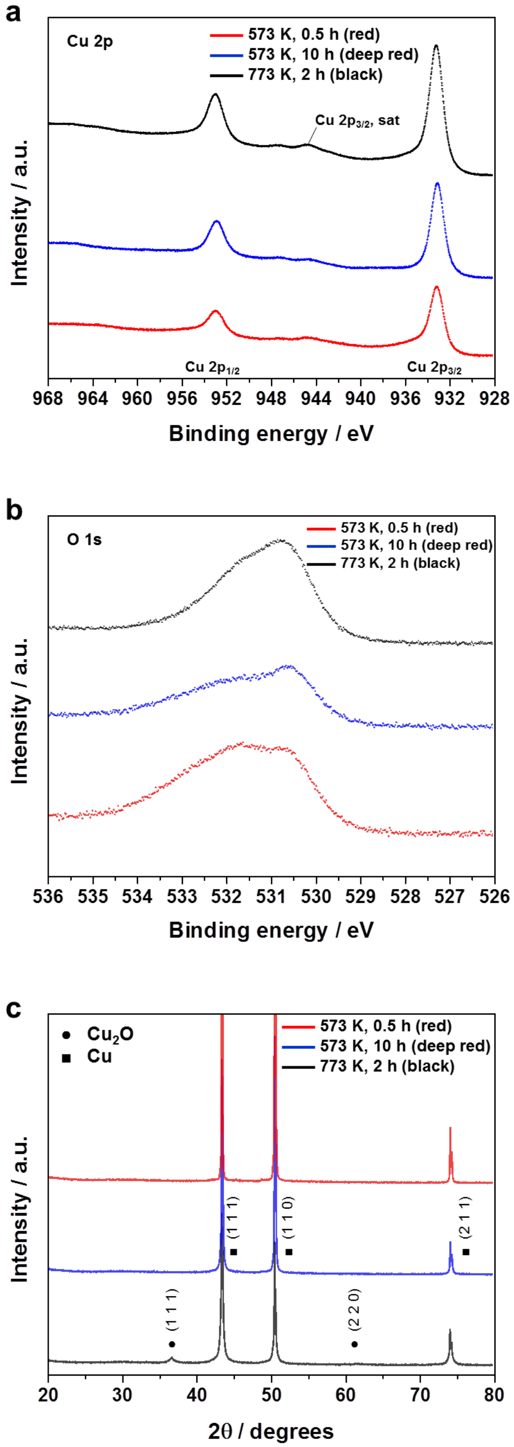

Fig. 9 (a) Cu 2p and (b) O 1s XPS spectra of the Cu-based electrodes after the electrocatalytic reduction of CO_2. (c) XRD patterns of the composite electrodes after exposure to the reductive reaction conditions. (1.67 mA cm^{-2}, 2 h, 0.1 M $KHCO_3$, CO_2 saturated, pH 6.8)

The morphology of the reduced Cu-based electrodes was studied *via* SEM, and the micrographs are shown in Figure 10. The formation of nanoparticles (< 10 nm) on the surfaces of the composite materials is observed for the red, deep red and black samples. The original texture and morphology of the pristine samples are mostly intact, but it is possible to observe increased surface roughness. The aggregates observed in the red sample are decreased in size (compare Figure 1d with 10a and Figure S1a with S9a), and smaller nanoparticles are homogenously distributed on the surface (see Figure S9b). A similar observation can be made for the deep red sample, where nanoparticles are clearly observed on the surfaces of the grains (Figure 9b) and the surface area seems to be higher because of the decrease in secondary-particle size (compare Figure S1c with Figure S9c and examine the details in Figure S1d and Figure S9d). The nanowires on the surfaces of the black

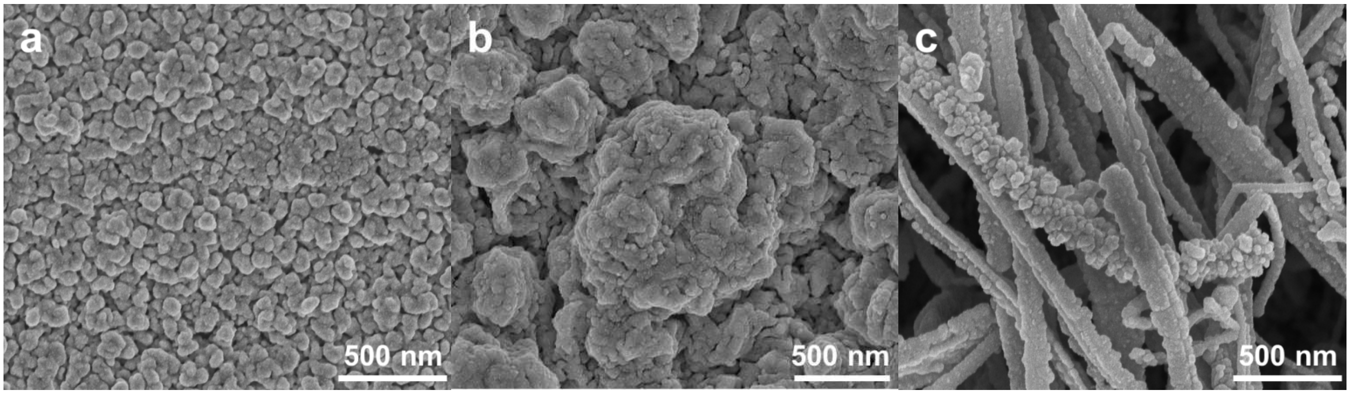

Fig. 10 Top SEM view of the (a) red, (b) deep red and (c) black samples treated under galvanostatic conditions for 2 h for the electrochemical reduction of CO_2. (1.67 mA cm^{-2}, 0.1 M $KHCO_3$, CO_2 saturated, pH 6.8)

samples are mostly covered by nanoparticles of various sizes (Figure 10c). The nanoparticles aggregated on the surfaces of the wires into larger particles while preserving the morphology, although with a small increase in the diameter of the nanowires (compare Figure S1f and Figure S9f). It follows that after the electrochemical reduction of CO_2, the surfaces of the oxides in contact with the electrolytes were gradually reduced and formed Cu nanoparticles homogeneously distributed on the surfaces of the electrodes, as confirmed by the XPS, XRD and SEM results. Impedance spectroscopy revealed a significant decrease in the charge-transfer resistance of the samples after the galvanostatic step, most likely an indication of the metallic state at the interface (compare Figure S3a and S3b).

Based on these observations, different Cu_2O thicknesses were obtained depending on the thermal-oxidation treatment. As the oxidizing treatment increased, a CuO layer and nanowires formed on the outer layer of the electrode and most likely functioned as a passivation layer. During the galvanostatic experiment, when the surface was activated for CO_2 reduction, CuO may have first reduced to Cu_2O[37], while Cu nanoparticles simultaneously formed on the surface, changing the solid-liquid interface. Moreover, once the metallic nanoparticles homogeneously covered most of the surface, the Cu_2O-electrolyte interface required for the reduction reaction was lost (Equation 1). It has been reported that an overpotential as high as −1.3 V relative to the Cu/Cu_2O reversible potential is required to completely reduce the oxide to metallic Cu in CO_2-saturated 0.5 M $KHCO_3$.[56] After the electrocatalytic test, bulk and surface characterizations of the black sample indicated the incomplete reduction of the underlying Cu_2O layer. Recent DFT calculations have shown the beneficial effect of oxygen impurities at the subsurface of Cu(111) improving the binding ability of CO_2 to the altered copper surfaces.[57] Based on the results, a certain threshold oxide thickness along with the CuO passivation layer may be required for the stabilization of such sites that are selectively active for CO_2 reduction. The coexistence of the metallic Cu state with Cu^+ cannot be ruled out for the reason of improved CO_2 reduction as demonstrated in this work.

Conclusions

We presented the use of a facile, versatile and scalable synthesis process to obtain copper oxide materials along with two different applications for solar fuel generation. First, we confirmed, using electrochemical methods, XRD, XPS, UV-Vis and SEM, the controlled formation of Cu_2O of various thicknesses *via* the careful variation of time and temperature conditions for the thermal oxidation of Cu foils. CuO nanowires can be formed on the surface of the Cu_2O under high oxidation temperature. The electrochemical stability and redox properties of the samples were evaluated at pH 7.9. We utilized impedance spectroscopy to estimate the energy-band diagrams and elucidate the semiconductive nature of each sample in contact with the electrolyte. As the treatment temperature increased, the carrier concentration in each sample increased (10^{18}-10^{19} cm^{-3}). Hence, a large electric field (≈ 10^6 V cm^{-1}) was formed at the interface. This electric field was significantly larger than the values previously reported in the literature. With extended thermal-oxidation treatments, a large positive shift in the flat-band potential was observed. The PEC evaluations of the pristine Cu-oxide-based photocathodes resulted in large photocurrents. The black samples produced photocurrents of 1 mA cm^{-2} at 0.5 V *vs.* RHE (pH 10.1). Furthermore, the photocurrent onset potential for the black sample was recorded at 0.8 V *vs.* RHE under alkaline conditions. The outstanding photoactivity of the as-obtained electrodes was attributed to the high crystallinity of the Cu_2O layer and the high carrier concentration, which generated a large electric field that provided efficient charge separation at the semiconductor-electrolyte interface. It is considered, however, that the photocurrents originate from the reduction of the oxide species at the electrolyte interface, requiring further protection of the surface for effective utilization to photo-induced catalysis. Second, we demonstrated that when the Cu-based-oxide materials were galvanostatically reduced, they can be used as effective electrocatalysts for the electrochemical reduction of CO_2 at low overpotential with good selectivity. Based on systematic characterization and the electrolysis results, we demonstrated that longer thermal-oxidation treatments lead to thicker Cu_2O/CuO layers, which are required to stabilize the active sites for selective CO_2 reduction. XRD and XPS spectroscopy provided evidence of the beneficial coexistence of Cu(I) and metallic copper for the selective reduction of CO_2.

Experimental

Cu-based electrodes

Cu foils (25 μm in thickness, 99.99%, Sigma-Aldrich) were first cut to the desired electrode size (1×3 cm) and cleaned for several minutes in 1 M HCl. The electrodes were then rinsed with Milli-Q water and dried. The Cu electrodes were tightly wrapped around glass microscope slides and inserted into a muffle furnace under ambient air conditions for thermal oxidation. This procedure was recently reported to produce non-flaking highly crystalline oxide samples in intimate contact with the Cu substrate.[58] The temperature and time of the electrode treatment were varied from 573 to 773 K and from 0.5 to 10 h, respectively. Electrical wires were attached to the backsides of the copper oxide samples, which were abraded to remove the surface oxide and to ensure ohmic, low-resistance contacts. Epoxy was applied to mask all but the active area of the copper oxide surface for further testing. An electrochemical-reduction step was further implemented for the experiments concerning the electrochemical reduction of CO_2.

Electrochemistry

All electrochemical and PEC procedures were performed using Milli-Q water (18 MΩ). Sodium sulfate (Na_2SO_4, ≥99.99%, Aldrich), sodium acetate (CH_3COONa, NaOAc, ≥99.0%, Sigma-Aldrich), sodium hydroxide (NaOH, 99.99%, Sigma-Aldrich), sulfuric acid (H_2SO_4, 99.999%, Aldrich) and potassium bicarbonate ($KHCO_3$, ≥99.99%, Sigma-Aldrich) were used as received to prepare the required electrolytes. All experiments were performed using a research-grade, multi-channel potentiostat (VMP3, BioLogic Science Instruments). A Pt wire and an Ag/AgCl (saturated KCl) electrode were used as the counter and reference electrodes, respectively. All experiments were recorded against this reference electrode, which was calibrated against an RHE. The results were then reported on the RHE scale using E (*vs*. RHE) = E (*vs*. Ag/AgCl) + 0.197 V + 0.0591 V*pH.

Cyclic voltammetry

The CV experiments were performed using a regular one-compartment electrochemical cell with a three-electrode configuration. Each Cu-oxide-based sample was used as the working electrode without further modification. During the experiments, it was ensured that only the desired active area was in contact with the electrolyte. The electrical contact was established by polishing one side of the electrode until a clean connection was obtained with the Cu underlayer. The CV results were recorded at 5 mV s^{-1} (except when noted) using a 0.1 M NaOAc solution (pH 7.9).

Impedance spectroscopy

The EIS was performed in the dark using a three-electrode cell and 0.1 M NaOAc (pH 7.9). The pH of the electrolyte was selected based on the Pourbaix diagram of Cu to increase the stability of the system. Moreover, the experimental potential range was selected based on the results obtained from the CV characterization (black lines in Figure 3) and considering the pH-potential thermodynamics. The samples generated Nyquist plots with characteristic depressed semicircles at fixed potentials, where no faradic processes were detected over a wide frequency range (0.1 Hz to 100 kHz, Figure S2). Thus, a modified Randles equivalent circuit with a constant-phase element was used to electrically approximate the semiconductor-electrolyte interface. The amplitude of the AC signal applied to the system was 10 mV, and the probed frequency range for the Mott-Schottky calculations was 1-100 kHz. Based on the frequency response (Figure S3), high frequency values were selected for the Mott-Schottky analysis (1-10 kHz).

Photoelectrochemistry

The characterization of the samples was performed in 0.5 M Na_2SO_4 (pH 4.9, adjusted with 2 M H_2SO_4) under simulated AM 1.5G solar irradiation calibrated to 60 mW cm^{-2} over the range 300-800 nm. The CV results were recorded at 10 mV s^{-1} under defined periods of dark and illuminated conditions. The PEC stability tests were recorded for the same electrolyte conditions (0.5 M Na_2SO_4, pH 4.9) and at a fixed potential (0.25 V *vs*. RHE) for 20 minutes with an illumination time of 20 s.

All electrolytes were purged for 30 minutes with Ar (99.9999 %) before and during the experiments (i.e., CV, EIS and PEC).

Electrochemical CO_2 reduction

The Cu-based electrodes were galvanostatically reduced with a constant current of −5 mA (exposed geometric area: 3 cm^2) in a 0.1 M $KHCO_3$ electrolyte saturated with CO_2 (pH 6.8). Chronopotentiometric signals were recorded during the galvanostatic reduction of the electrode. The CO_2 electro-reduction experiments were performed in an airtight, two-compartment electrochemical cell. The Pt-wire counter electrode was isolated from the main cell using a ceramic frit, and the same electrolyte was used in both compartments. The cathodic compartment was saturated with CO_2 (99.995%) at 5 sccm for 30 minutes before and during the electrolysis runs. The gas mixture was delivered directly to the sampling loop of a gas chromatograph (μGC, T-3000 SRI instruments). Sampling points were collected every 3 minutes, and the gaseous products were analyzed using packed MolSieve 5A and packed HaySep Q columns coupled with thermal conductivity detectors (TCD). Ar (99.9999%) and He (99.9999%) were used as the carrier gases for the analysis. The liquid products (HCOOH and CH_3COOH) were analyzed using a high-pressure liquid chromatography (HPLC, Agilent technologies) system equipped with Agilent 1200, 1260 and 1290 Infinity liquid chromatography technology. All experiments were performed at room temperature (298 K) and under atmospheric conditions (101.3 kPa).

Notes and references

[a] Division of Physical Sciences and Engineering, KAUST Catalysis Center (KCC), King Abdullah University of Science and Technology (KAUST), 4700 KAUST, Thuwal, 23955-6900 Saudi Arabia. E-mail: kazuhiro.takanabe@kaust.edu.sa
[b] Department of Mechanical Engineering, University of California, Berkeley, California 94720, USA.
[c] Département Chimie Physique, Stockage et Conversion de l'énergie (SCE), École Nationale Supérieure de Chimie, de Biologie et de Physique (ENSCBP), Pessac 33607, France.

† Electronic Supplementary Information (ESI) available. See DOI: 10.1039/b000000x/

‡ These authors contributed equally to this work.

1 A. Harriman, *Philos. Trans. A. Math. Phys. Eng. Sci.*, 2013, **371**, 20110415.
2 K. Takanabe and K. Domen, *Green*, 2011, **1**, 313–322.
3 Z. Chen, T. F. Jaramillo, T. G. Deutsch, A. Kleiman-Shwarsctein, A. J. Forman, N. Gaillard, R. Garland, K. Takanabe, C. Heske, M. Sunkara, E. W. McFarland, K. Domen, E. L. Miller, J. A. Turner, and H. N. Dinh, *J. Mater. Res.*, 2011, **25**, 3–16.

4 S. C. Roy, O. K. Varghese, M. Paulose, and C. A. Grimes, *ACS Nano*, 2010, **4**, 1259–1278.

5 T. L. Frölicher, M. Winton, and J. L. Sarmiento, *Nat. Clim. Chang.*, 2014, **4**, 40–44.

6 G. Centi, E. A. Quadrelli, and S. Perathoner, *Energy Environ. Sci.*, 2013, **6**, 1711–1731.

7 Y. Chen and M. W. Kanan, *J. Am. Chem. Soc.*, 2012, **134**, 1986–1989.

8 A. Paracchino, V. Laporte, K. Sivula, M. Grätzel, and E. Thimsen, *Nat. Mater.*, 2011, **10**, 456–461.

9 M. G. Walter, E. L. Warren, J. R. McKone, S. W. Boettcher, Q. Mi, E. a Santori, and N. S. Lewis, *Chem. Rev.*, 2010, **110**, 6446–6473.

10 A. Paracchino, J. C. J. Brauer, J.-E. Moser, E. Thimsen, and M. Graetzel, *J. Phys. Chem. C*, 2012, **116**, 7341–7350.

11 C. G. Morales-Guio, S. D. Tilley, H. Vrubel, M. Grätzel and X. Hu, *Nat. Commun.*, 2014, **5**, DOI: 10.1038/ncomms4059.

12 C. Li, Y. Li, and J.-J. Delaunay, *ACS Appl. Mater. Interfaces*, 2014, **6**, 480–486.

13 Z. Zhang and P. Wang, *J. Mater. Chem.*, 2012, **22**, 2456.

14 P. E. De Jongh, D. Vanmaekelbergh, and J. J. Kelly, *Chem. Mater.*, 1999, **11**, 3512–3517.

15 A. Morales-Acevedo, K. Akimoto, S. Ishizuka, M. Yanagita, Y. Nawa, G. K. Paul, and T. Sakurai, *Sol. Energy*, 2006, **80**, 715–722.

16 S. Ishizuka, T. Maruyama, and K. Akimoto, *Jpn. J. Appl. Phys.*, 2000, **39**, L786–L788.

17. D. P. Singh, N. R. Neti, A. S. K. Sinha, and O. N. Srivastava, *J. Phys. Chem. C*, 2007, **111**, 1638–1645.

18 F. Caballero-Briones, J. M. Artés, I. Díez-Pérez, P. Gorostiza, and F. Sanz, *J. Phys. Chem. C*, 2009, **113**, 1028–1036.

19 Y. Tan, X. Xue, Q. Peng, H. Zhao, T. Wang, and Y. Li, *Nano Lett.*, 2007, **7**, 3723–3728.

20 L. Gou and C. J. Murphy, *Nano Lett.*, 2003, **3**, 231–234.

21 M. S. Prévot and K. Sivula, *J. Phys. Chem. C*, 2013, **117**, 17879–17893.

22. D. T. Whipple and P. J. A. Kenis, *J. Phys. Chem. Lett.*, 2010, **1**, 3451–3458.

23 C. W. Li and M. W. Kanan, *J. Am. Chem. Soc.*, 2012, **134**, 7231–7234.

24 Y. Chen, C. W. Li, and M. W. Kanan, *J. Am. Chem. Soc.*, 2012, **134**, 19969–19972.

25 X. Jiang, T. Herricks, and Y. Xia, *Nano Lett.*, 2002, **2**, 1333–1338.

26 K. Mizuno, M. Izaki, K. Murase, T. Shinagawa, M. Chigane, M. Inaba, A. Tasaka, and Y. Awakura, *J. Electrochem. Soc.*, 2005, **152**, C179–C182.

27 N. S. McIntyre, *J. Vac. Sci. Technol.*, 1981, **18**, 714.

28 C.-K. Wu, M. Yin, S. O'Brien, and J. T. Koberstein, *Chem. Mater.*, 2006, **18**, 6054–6058.

29 S. Poulston, P. M. Parlett, P. Stone, and M. Bowker, *Surf. Interface Anal.*, 1996, **24**, 811–820.

30 M. Yin, C.-K. Wu, Y. Lou, C. Burda, J. T. Koberstein, Y. Zhu, and S. O'Brien, *J. Am. Chem. Soc.*, 2005, **127**, 9506–9511.

31 A. E. Rakhshani, *Solid. State. Electron.*, 1986, **29**, 7–17.

32 T. D. Golden, M. G. Shumsky, Y. Zhou, R. A. VanderWerf, R. A. Van Leeuwen, and J. A. Switzer, *Chem. Mater.*, 1996, **8**, 2499–2504.

33 M. Heinemann, B. Eifert, and C. Heiliger, *Phys. Rev. B*, 2013, **87**, 115111.

34 C. J. Engel, T. A. Polson, J. R. Spado, J. M. Bell, and A. Fillinger, *J. Electrochem. Soc.*, 2008, **155**, F37–F42.

35 J. Ambrose, R. G. Barradas, and D. W. Shoesmith, *J. Electroanal. Chem. Interfacial Electrochem.*, 1973, **47**, 47–64.

36 J. M. M. Droog, C. A. Alderliesten, P. T. Alderliesten, and G. A. Bootsma, *J. Electroanal. Chem. Interfacial Electrochem.*, 1980, **111**, 61–70.

37 S. Nakayama, A. Kimura, M. Shibata, S. Kuwabata, and T. Osakai, *J. Electrochem. Soc.*, 2001, **148**, B467–B472.

38 S. Nakayama, T. Kaji, M. Shibata, T. Notoya, and T. Osakai, *J. Electrochem. Soc.*, 2007, **154**, C1-C6.

39 S. T. Mayer, *J. Electrochem. Soc.*, 1992, **139**, 426–434.

40 R. Babić, M. Metikoš-Huković, and M. Lončar, *Electrochim. Acta*, 1999, **44**, 2413–2421.

41 M. Metikoš-Huković, R. Babić, and I. Paić, *J. Appl. Electrochem.*, 2000, **30**, 617–624.

42 P. E. de Jongh, D. Vanmaekelbergh, and J. J. Kelly, *Chem. Commun.*, 1999, 1069–1070.

43 K. Gelderman, L. Lee, and S. W. Donne, *J. Chem. Educ.*, 2007, **84**, 685–688.

44 F. P. Koffyberg, *J. Appl. Phys.*, 1982, **53**, 1173–1177.

45 E. Heltemes, *Phys. Rev.*, 1966, **141**, 803–805.

46 A. D. Handoko and J. Tang, *Int. J. Hydrogen Energ.*, 2013, **38**, 13017–13022.

47 J. W. Hodby, T. E. Jenkins, C. Schwab, H. Tamura, and D. Trivich, *J. Phys. C Solid State Phys.*, 1976, **9**, 1429–1439.

48 W. Schmickler and E. Santos, in *Interfacial electrochemistry*, Springer Berlin Heidelberg, Berlin, Heidelberg, 2nd Editio., 2010, vol. 131, pp. 117–131.

49 F. Orecchini, J.-N. Nian, C.-C. Hu, and H. Teng, *Int. J. Hydrogen Energy*, 2008, **33**, 2897–2903.

50 S. D. Tilley, M. Schreier, J. Azevedo, M. Stefik, M. Grätzel, *Adv. Funct. Mater.*, 2014, **24**, 303–311.

51 C-Y. Lin, Y-H. Lai, D. Mersch and E. Reisner, *Chem. Sci.*, 2012, **3**, 3482–3487.

52 B. Seger, T. Pedersen, A. B. Laursen, P. C. K. Vesborg, O. Hansen and I. Chorkendorff, *J.Am.Chem. Soc.*, 2013, **135**, 1057–1064.

53 Z. Zhang, R. Dua, L. Zhang, H. Zhu, H. Zhang, and P. Wang, *ACS Nano*, 2013, **7**, 1709–1717.

54 A. Paracchino, N. Mathews, T. Hisatomi, M. Stefik, S. D. Tilley, and M. Grätzel, *Energy Environ. Sci.*, 2012, **5**, 8673–8681.

55 W. Tang, A. A. Peterson, A. S. Varela, Z. P. Jovanov, L. Bech, W. J. Durand, S. Dahl, J. K. Nørskov, and I. Chorkendorff, *Phys. Chem. Chem. Phys.*, 2012, **14**, 76–81.

56 M. Le, M. Ren, Z. Zhang, P. T. Sprunger, R. L. Kurtz, and J. C. Flake, *J. Electrochem. Soc.*, 2011, **158**, E45–E49.

57 J. Xiao, T. Frauenheim, A. Kuc and T. Heine, *J. Mater. Chem. A*, 2014, DOI: 10.1039/C3TA14755J.

58 F. Mumm and P. Sikorski, *Nanotechnology*, 2011, **22**, 105605.

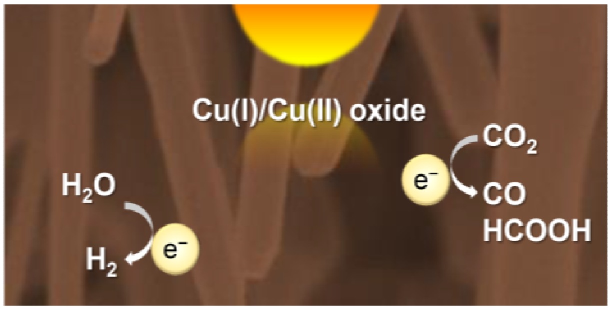

TOC

Thorough characterization has been conducted on thermally obtained Cu(I)/Cu(II) oxide (photo)electrodes for applications of solar fuel generation.